AIAA JOURNAL
Vol. 45, No. 8, August 2007

Planar Velocimetry of Jet/Fin Interaction on a Full-Scale Flight Vehicle Configuration

Steven J. Beresh*
Sandia National Laboratories, Albuquerque, New Mexico 87185
and
James T. Heineck,† Stephen M. Walker,‡ Edward T. Schairer,§ and David M. Yaste¶
NASA Ames Research Center, Moffett Field, California 94035

DOI: 10.2514/1.26485

Stereoscopic particle image velocimetry has been implemented in a production-scale transonic wind tunnel for studying jet/fin interaction created by exhaust plumes from spin rockets on a full-scale model of a finned body of revolution. Data acquired just upstream of the leading edge of the fin root clearly display the counter-rotating vortex pair that dominates the interaction far field and the remnant of the horseshoe vortex near the vehicle surface. The counter-rotating vortex pair is distinctly asymmetric due to originating from a scarfed nozzle and displays some rotation with respect to the model surface. Velocity fields measured over a range of flowfield conditions and model orientations show that the vortex of negative sign is always closer to the fins than its positive counterpart and does not greatly change location as flowfield parameters are altered. The circulation of this vortex correlates with a reduction in the simultaneously measured vehicle roll torque. Further correlations are hindered by untreatable bias errors in the velocimetry. Instead, a model of the vortex structure derived from the velocimetry data reveals that the angle of attack induced upon the fins by the counter-rotating vortex pair correlates with the roll torque loss. Similar correlations suggest that in level flight this effect is dominant, but at angle of attack the horseshoe vortex on the windward side has an additional influence.

Nomenclature

A_0	=	maximum cross-sectional area of the flight vehicle
a	=	vortex model constant for the vortex strength
b	=	vortex model constant for the vortex size
C_{CT}	=	countertorque coefficient, determined from the aerodynamic balance
$C_{RM,v}$	=	countertorque coefficient, determined from velocimetry measurements
d_j	=	jet nozzle exit diameter, measured on the nozzle centerline
d_x	=	diameter of the flight vehicle at the location of the particle image velocimetry measurement plane
d_Γ	=	diameter of a vortex
d_0	=	maximum diameter of the flight vehicle
J	=	jet-to-freestream dynamic pressure ratio
M_∞	=	freestream Mach number
q_∞	=	freestream dynamic pressure
r	=	distance from some point to a vortex center
s	=	distance from a vortex center to the origin of the coordinate axes
U_∞	=	freestream velocity
α	=	vehicle angle of attack
α_{fin}	=	induced angle of attack on a fin
Γ_x	=	circulation of a vortex
ω_x	=	vorticity

Received 11 July 2006; revision received 27 December 2006; accepted for publication 24 January 2007.

*Principal Member of the Technical Staff, Engineering Sciences Center, P. O. Box 5800, Mailstop 0834; sjberes@sandia.gov. Senior Member AIAA.
†Photographic Technologist, Experimental Aerophysics Branch, MS260-1.
‡Aerospace Engineer, Experimental Aerophysics Branch, MS260-1. Member AIAA.
§Aerospace Engineer, Experimental Aerophysics Branch, MS260-1.
¶Engineering Technologist, Experimental Aerophysics Branch, MS260-1.

Introduction

ATMOSPHERIC flight vehicles that employ supersonic jets for attitude or roll control may find their expected performance altered due to an interaction between the exhausting jet and downstream control surfaces. Once the jet exits from the nozzle, it is reoriented by its encounter with the crossflowing freestream and travels aft where it can influence the pressure field on the fins and hence the force they generate [1–6]. The far field of the interaction is dominated by the presence of a counter-rotating vortex pair (CVP) initially generated when the jet exhausts into the crossflow, which is believed to be principally responsible for the interaction with downstream fins through the mechanism illustrated in Fig. 1 (modified from [7]). The rotational flow produced by the CVP and a secondary vortex system near the surface modifies the pressure field on the fins, creating a countertorque that opposes the direction of the spin rockets. Knowledge of the structure of this vortex system is largely extrapolated from low-speed studies in which measurements are more easily made (for example, [8–10]), but these vortices have been directly detected in compressible flowfields as well [11–13].

As a means of acquiring countertorque measurements to predict in-flight performance, a wind-tunnel experiment was conducted on a full-scale model of a flight vehicle in which the spin rockets were simulated using high-pressure air and the vehicle's aerodynamic response was measured using an internal strain-gage balance, described in detail in [7]. The resulting database assessed the dependency of these countertorques on the flowfield conditions, model orientation, and various model geometries. Although these measurements provided data necessary to vehicle design, they offered only limited physical insight into the nature of jet/fin interaction or why the countertorques vary as they do with flight parameters, and thus this experiment did not yield a means of predicting the effects of jet/fin interaction in a manner broadly applicable to a variety of vehicles and configurations. Such a predictive capability could emerge from an approach designed to yield a high-fidelity data set that can more fully elucidate the underlying fluid mechanics of the problem.

To address this need, a subsequent experiment has been conducted using the same model in a similar production-scale wind tunnel in which flowfield velocimetry measurements were acquired of the jet interaction using stereoscopic particle image velocimetry (PIV) simultaneous with aerodynamic data from the balance. By employing these velocity fields to define the strength, size, and position of the induced vortices over a range of flowfield conditions and vehicle orientations, then comparing these key interaction parameters with the aerodynamic forces experienced by the vehicle, an improved understanding of the nature of jet/fin interaction is anticipated. Such measurements additionally provide the fidelity for use in improving computational simulations beyond that possible solely with integrated quantities such as countertorque measurements. Whereas PIV data acquired in related subscale experiments [13–15] are important for the development and validation of the underlying physical models, similar data gathered for the full-scale flight vehicle provide a more extensive test of the simulation capability despite the limitations of flowfield diagnostics in a production-scale facility. Moreover, simplified predictive models applicable to parametric studies for vehicle design may become feasible if a causal relationship can be established between the vortical system established by firing the spin rockets and the aerodynamic response of the vehicle.

Experimental Apparatus

Wind Tunnel

The experiment was performed in the NASA Ames 11-Foot Unitary Plan Wind Tunnel. This facility is a variable-pressure, closed-circuit, continuous-flow tunnel possessing slotted walls for transonic operation whose test section is 3.4×3.4 m^2 (11×11 ft^2) and 6.7 m (22 ft) long. The two side walls each contain windows 3.2 m (126 in.) long and 1.94 m (49.5 in.) tall, divided into panes 1.04 m (41 in.) long and 0.19 m (7.5 in.) tall by the ventilation slots. Windows not needed for the PIV measurements were painted black to reduce background light reflection. The tunnel's model support mechanism combines pitch and translation to allow pitching about an arbitrary center, but yaw is necessarily fixed on the knuckle's center of rotation. Auxiliary air of up to 20 MPa and 18 kg/s (3000 psi and 40 lb/s) was passed through the sting and used to supply the model's spin rockets, as described below.

Flight Vehicle Model

The wind-tunnel model was a full-scale reproduction of a flight vehicle whose geometry is a body of revolution possessing four equally spaced aft fins. Two supersonic spin rockets are located at approximately the model midsection, in 180 deg opposition, and canted at 39.5 deg with respect to the surface normal such that a torque is generated about the longitudinal axis. A cutaway view of the model body is drawn in Fig. 2. The body itself is about 3.6 m (12 ft) in length from the nose to the fin trailing edge with a maximum diameter of 0.34 m (13.3 in.). The vehicle's aft body is boat-tailed and the spin rockets are located at the maximum diameter of the body; therefore the fin roots are situated slightly closer to the body centerline than the rockets. On the actual flight vehicle, the fins are canted with respect to the freestream to provide roll torque (which is complemented by the spin rockets), but because fin cant is of minimal significance to the measured countertorque [7], the wind-tunnel model exclusively uses uncanted fins for the PIV experiments.

The nozzles for the spin rockets are scarfed by the cylindrical surface of the vehicle body, creating a nonuniform Mach number distribution across the exit plane, with a nominal centerline Mach number of 3.66 and an effective nozzle diameter at this point of 38.2 mm (1.50 in.). This is sketched in Fig. 3. Exit Mach numbers vary from 3.15 on the short edge to 4.36 on the long edge. Rather than the hot combustion gases present in the actual flight vehicle, the nozzle flow was simulated by room-temperature high-pressure air. The nozzle throat diameter was altered from the flight article to provide the same centerline Mach number despite the change in the specific-heat ratio. The stagnation chamber for each nozzle is instrumented for pressure and temperature measurements.

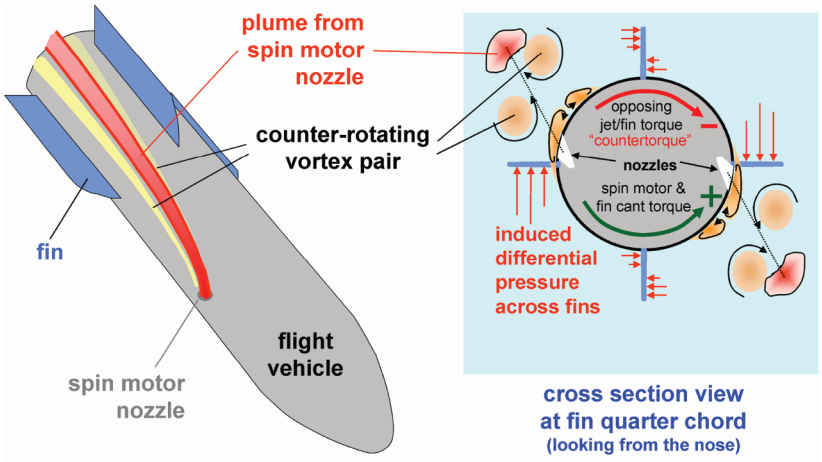

Fig. 1 Illustration of jet/fin interaction, in which vortices generated by the jet-in-crossflow interaction induce pressures on the fins to create a countertorque opposing the torque generated by the spin rockets (from [7]).

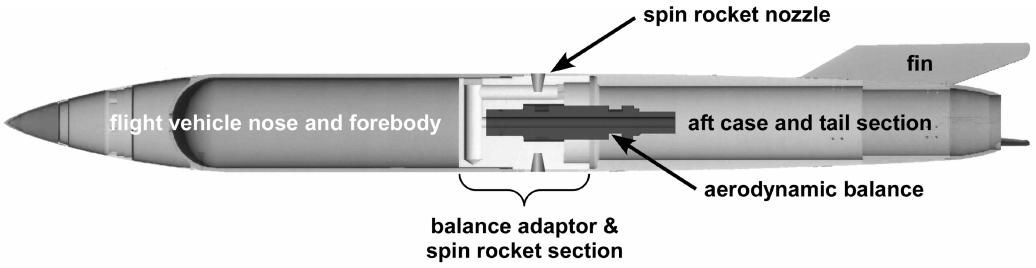

Fig. 2 Full-scale wind-tunnel model (from [7]).

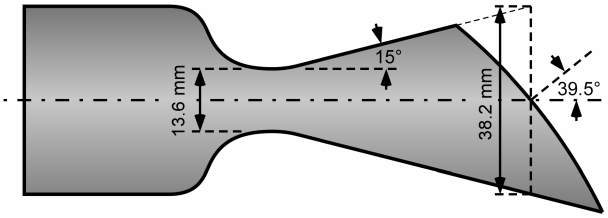

Fig. 3 Spin-rocket nozzle geometry.

All PIV data were acquired with the model oriented at the same roll angle, which placed the fins at the 45 deg positions (i.e., the "X" configuration). This located the center of each nozzle exit plane 101 mm (3.97 in.) laterally from the model pitching plane, with the thrust vector canted 3.5 deg inward (sketched in subsequent data figures).

Force and moment measurements were made using a five-component aerodynamic balance furnished by Arnold Engineering and Development Center, which has the capability to pass high-pressure air through its centerline and acquire all but the axial force while operating the jets.

Particle Image Velocimetry System

Stereoscopic PIV measurements were acquired using the arrangement sketched in Fig. 4. The laser sheet was projected from one side of the wind tunnel and aligned to a plane normal to the longitudinal vehicle axis about 50 mm (2.0 in.) upstream of the leading edge of the fin root, as seen in the photograph in Fig. 5. This position is 820 mm (32.3 in.) downstream of the centerline of the spin rockets. Cameras were situated on the opposite side of the test section, one viewing the laser sheet from the front and one from the back, each at an angle of 33 deg to the laser sheet. This arrangement allowed the cameras to capture images largely in forward scatter and hence improve the efficiency of light collection. Both the cameras and the final turning mirror for the laser sheet were placed on translation stages such that the entire apparatus could be moved in tandem, thus relocating the position of the measurement plane without necessitating a recalibration. In addition to the measurement station just upstream of the fins, a second measurement station was located 406 mm (16.0 in.) farther upstream, placing it 414 mm (16.3 in.) downstream of the nozzle centerlines. The position of this upstream station was limited by the maximum traverse of the translation stages.

Fig. 5 Photograph of the laser sheet position relative to the wind-tunnel model.

The PIV system employed four Nd:YAG lasers operating at 532 nm (New Wave Gemini 120). Two lasers each were timed for the initial and delayed pulses, allowing greater energy (about 220 mJ per pulse). The delayed laser beam was placed on a remotely actuated traverse to allow the laser sheet to be displaced downstream from the initial sheet. In conjunction with the proper selection of the time between laser pulses, this sheet separation was chosen to account for the out-of-plane motion of the particles while permitting a greater dynamic range for the in-plane velocity measurements. This arrangement improves upon simply using thickened coplanar sheets because it does not raise the background noise of the measurement by introducing additional uncorrelated particle pairs. The initial upstream sheet was 1.5 mm thick and the delayed downstream sheet was 3.0 mm thick. The time between laser pulses varied from 3.25–5.50 μs and the sheet separation distance from 0.7–0.9 mm; these values were adjusted to accommodate different flow conditions.

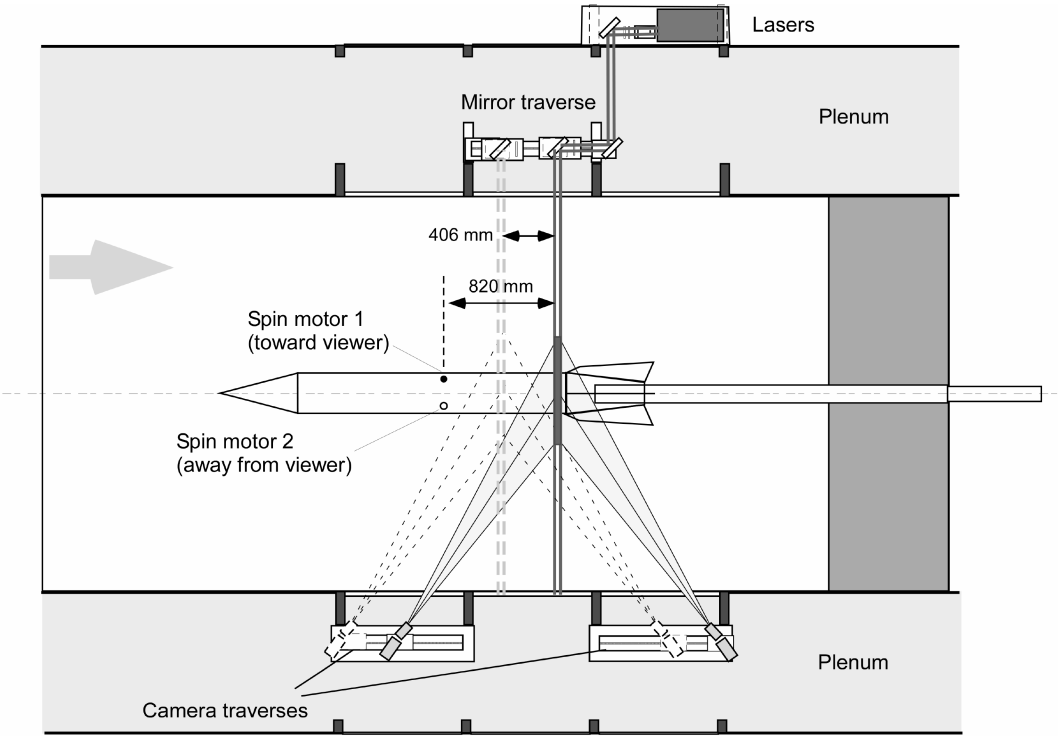

Fig. 4 Schematic of the stereoscopic PIV system in the NASA Ames 11-Foot Unitary Wind Tunnel.

Scattered laser light was captured with 2048×2048 pixel frame-straddling cameras (Redlake MegaPlus ES4.0) with 85 mm lenses placed on Scheimpflug mounts to achieve an oblique focal plane. The cameras were located within the plenum of the wind tunnel and operated successfully despite the reduced ambient pressure. The platforms on which they were mounted were secured against wind-tunnel vibrations. The field of view was about 0.4 m (16 in.) tall at the model centerline and spanned about 0.9 m (36 in.).

The tunnel was seeded by two thermal smoke generators (Corona Vi-Count 5000) that produce from a mineral oil base a large quantity of particles typically 0.2–0.5 μm in diameter. Exhausting smoke was ducted to the downstream end of the test section, which eventually recirculated the particles through the closed-loop tunnel; achieving the desired particle density was simply a matter of running the smoke generator until a sufficient quantity of particles accumulated. The jet itself was not seeded, but all PIV measurements were taken far enough downstream of the jet nozzles that turbulent mixing had entrained particles throughout the jet interaction and removed any sampling bias that would be found near the jet exit. The particles were sufficiently small that they rapidly attained the local velocity once they had been redistributed [16,17].

Calibration of the two cameras was accomplished using the distorted sheet procedure [18], also known as a "thick sheet" or multiplane calibration, by placing into the measurement plane an aluminum plate drilled with fiduciary holes. Both surfaces of the plate had been sandblasted to create speckle patterns when illuminated, upon which the PIV software can correlate as the plate is translated through the measurement region. Green LED lamps were used for illumination during the calibration process as they were found to provide sharper speckle patterns than white light, as well as providing a narrow wavelength that nearly matched that of the laser to ensure no refocusing due to chromatic aberration. The target was mounted upon translation and rotation stages set on a tripod temporarily placed in the test section, then precisely aligned with the laser sheet. A series of images was acquired as the target was translated through the laser sheet volume, which were employed by the calibration algorithm to tie together the two sets of image pairs with the physical space they view to produce a plane of three-dimensional vectors. Because the PIV system was calibrated to a fixed location within the wind tunnel, all data were acquired using the same field of view but vertically translating the model within it as flowfield conditions or model pitch altered the position of the vortices under study. Additionally restrictions on the model roll capability coupled with the immobility of the PIV system dictated that only the interaction produced by the upper nozzle could be studied and that data analysis would assume symmetry between the two nozzles.

HeNe lasers were placed just outside the plenum opposite the cameras and directed onto targets applied to the windows, positioned such that one laser spot was visible at the far edge of each PIV image, outside the useful field of view. These HeNe spots were monitored during the course of wind-tunnel operation to ensure that they remained in the same position; a shift would have indicated a movement in the camera alignment (as the HeNe's were outside the plenum, their movement was less likely). Similarly a target was placed on the window where the Nd:YAG laser sheet impinged and viewed through neutral density filters by a monitor camera to determine if the laser sheet drifted. These alignment monitors were used to detect if any alignment or calibration needed to be repeated, avoiding the need for unnecessary precautionary actions that would have been expensive in a production-scale wind tunnel.

Sequences of 100 image pairs were acquired for each set of flow conditions and model orientation. Data were processed using IDT's ProVision 2.02 with adaptive correlations and an image offset to account for the streamwise particle displacement, usually on a 32×32 pixel interrogation window but some analysis required use of a 64×64 pixel window as discussed below. Adjacent interrogation windows overlapped by approximately 50% to oversample the images. Validated vector fields were collapsed into mean data for each case. The spatial resolution varies laterally across the vector fields due to the oblique view, but at the wind-tunnel centerline it is 13 mm laterally and 7 mm vertically.

Operating Conditions

PIV datasets were acquired while varying such parameters as J, M_∞, q_∞, and α. About 60 sets of conditions were studied; however in the interest of brevity, the present document discusses only a subset of these. In particular, the vector plots shown are limited to those where $q_\infty = 21.2$ kPa (3.08 psia), corresponding to wind-tunnel stagnation pressures of 47.2, 33.5, and 25.0 kPa (6.85, 4.86, and 3.62 psia) at $M_\infty = 0.8$, 0.95, and 1.1, respectively. This provides a wind-tunnel unit Reynolds number of 9.2×10^6 m^{-1} (2.8×10^6 ft^{-1}) at $M_\infty = 0.8$, falling to 8.2×10^6 m^{-1} and 7.5×10^6 m^{-1} (2.5×10^6 ft^{-1} and 2.3×10^6 ft^{-1}) at $M_\infty = 0.95$ and 1.1, respectively. The wind-tunnel stagnation temperature was 296 K $\pm$ 4 K (532°R $\pm$ 8°R), providing freestream velocities of $U_\infty = 260$ m/s, 302 m/s, and 342 m/s for $M_\infty = 0.8$, 0.95, and 1.1, respectively. To achieve the desired values of $J = 8$, 16, and 36, jet stagnation pressures of 1.45, 2.83, and 6.34 MPa (210, 410, and 920 psia), respectively, were established while the jet stagnation temperature remained nominally constant at 306 K (550°R). Each case was run at $\alpha = 0$ and ± 4 deg for each combination of J and M_∞. Where $M_\infty = 1.1$ and $J = 36$, the wind tunnel was unable to fully evacuate the added mass from the jets, and therefore the Mach number fell to $M_\infty = 1.06$.

Results and Discussion

Countertorque Measurements

Before the acquisition of PIV data, aerodynamic data were acquired from the balance to complement that gathered previously in a different wind tunnel [7]. These data were principally intended to examine the countertorque due to the jet/fin interaction; that is, the magnitude of the loss in roll torque associated solely with the interaction. The countertorque coefficient is found as

$$C_{CT} = \frac{-(T - T_j - T_f)}{q_\infty A_0 d_0} \tag{1}$$

where T is the total roll torque measured by the balance; T_j is the roll torque from the jets alone, found with the wind tunnel off; and T_f is the roll torque from the fins (zero for uncanted fins), found with the jets off. Figure 6 plots the countertorque curves for those conditions studied by PIV at $q_\infty = 21.2$ kPa as a function of J; data circles represent the conditions at which PIV measurements were acquired. Countertorque curves were gathered only for $\alpha = 0$ and $+4$ deg, assuming symmetry with $\alpha = -4$ deg. However earlier aerodynamic tests showed that this was not strictly true in some cases.

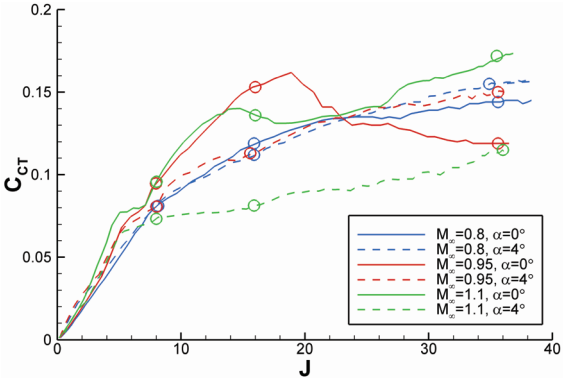

Fig. 6 Countertorque coefficient for the reduction in roll torque due to jet/fin interaction at $q_\infty = 21.2$ kPa. Data circles show conditions at which PIV measurements were acquired.

From Fig. 6, it is apparent that at $M_\infty = 0.8$, the countertorque monotonically increases with greater J, and that increasing α from 0 to 4 deg makes relatively little difference. This is not the case for $M_\infty = 0.95$ and $M_\infty = 1.1$, however, where striking changes to the slope of the countertorque curve are evident and substantial differences arise due to the shift in angle of attack. Though not shown in Fig. 6, changes in q_∞ did not have an appreciable effect at $M_\infty = 0.8$ but produced markedly different curves at $M_\infty = 0.95$ and $M_\infty = 1.1$; this is consistent with the previous experiment [7]. Dependence upon q_∞ is beyond the scope of this paper and not discussed further. The points at which PIV data were acquired have been selected to attempt to discover alterations in the flowfield structure that may explain the deviations between the countertorque curves in Fig. 6.

Downstream Velocity Fields

Stereoscopic PIV data acquired for $M_\infty = 0.8$ are shown in Fig. 7 for five of the nine combinations of $\alpha = 0$ and ± 4 deg with $J = 8$, 16, and 36 at the measurement station 50 mm (2.0 in.) upstream of the leading edge of the fin root; those omitted for brevity bear a strong resemblance to those already shown. Figure 7 displays the mean vector fields, looking from aft of the vehicle forward. Vectors show the in-plane velocity components, whereas the contour plot reveals the out-of-plane motion, where the in-plane vectors have been subsampled by a factor of 2 in each direction for visual clarity. The coordinate system is chosen such that x is in the direction of the wind-tunnel freestream, y is horizontal, and z is vertical; these axes are coincident with the model body coordinate system when the model is at $\alpha = 0°$. The axes have been normalized to d_j (see Fig. 3) and velocities are normalized to U_∞, the latter of which is determined from the wind-tunnel flow conditions and not the PIV measurements. The position of the wind-tunnel model also is provided in Fig. 7; the dashed circle shows the diameter of the model at the axial station where the jet nozzles are located, whereas the solid circle shows the reduced diameter at the measurement position due to the boat-tailed geometry. The fin locations are displayed as well, although they lie downstream of the measurement plane.

The principal condition at which the jet/fin interaction was studied is $M_\infty = 0.8$, $J = 16$, and $\alpha = 0$ deg, which is shown in Fig. 7b. The primary vortex pair is clearly visualized both by the in-plane rotation and by the out-of-plane velocity deficit; this is the counter-rotating vortex pair (CVP) indelibly associated with jet interactions. In addition, a smaller vortex pair can be seen near the surface of the model, which is the remnant of the horseshoe vortex (HSV) known to wrap around the jet as it exits from the nozzle. The HSV is displaced from the lateral position of the nozzle exit, and the CVP displays some rotation such that an imaginary line connecting the two vortices is no longer oriented parallel to the surface as it is for an interaction generated by an axisymmetric nozzle under similar flow conditions [13]. The CVP is conspicuously asymmetric, with the upper vortex displaying a larger streamwise velocity deficit than the lower vortex. This likely arises from the asymmetry of the jet nozzle itself, whose lateral variations in the jet Mach number effectively alter the J parameter across the interaction. The resulting unequal vortex rotation twists the vortices as they extend downstream while displacing the HSV laterally from its origin at the nozzle. Figure 7b also displays a weak, narrow wake extending from the CVP toward the HSV, which is similar to that detected in a symmetric jet interaction [13].

As the value of J is altered, the scale of the interaction shifts accordingly. Figures 7a and 7e demonstrate that the same basic structure persists at $J = 8$ and $J = 36$, but the size of the vortices and magnitude of the streamwise velocity deficit are a strong function of J, as is the distance of the CVP from the surface of the model. The interaction for the $J = 36$ case is large enough that two passes with the PIV instrument were necessary with the model vertically translated between them, then the resulting vector fields were stitched together; the mismatch between velocity values at the seam is within the measurement uncertainty (see below).

Figures 7c and 7d show the effects of pitching the model to $\alpha = \pm 4$ deg. Assuming symmetry of the interactions produced by the two spin-rocket nozzles, Fig. 7c displays the vehicle's leeward vortices whereas Fig. 7d shows the windward side, although in practice, all data were acquired from the same nozzle with the model pitched both positive and negative. As can be seen, the leeward CVP in Fig. 7c looks much the same as that for $\alpha = 0$ deg in Fig. 7b and is located in approximately the same position relative to the nozzle exit. In contrast, the windward CVP in Fig. 7d shows a much smaller streamwise velocity deficit, although the in-plane vortical rotation appears similar to that in Figs. 7b and 7c. The leeward HSV in Fig. 7c is similar in size and strength to that in Fig. 7b, at least to within the measurement uncertainty near the model surface, whereas the windward HSV in Fig. 7d is distinctly weaker.

The velocity data of Fig. 7 all display common measurement biases. The contour scale of the out-of-plane velocity component clearly indicates that the PIV measurement of the freestream velocity exceeds the value of U_∞ determined from the wind-tunnel flow conditions. Furthermore, each plot shows an artificial reduction in streamwise velocity near the upper edge (though it is not equally evident in each case). The lower left corner of each vector field displays a group of vectors directed toward $+y$ and $+z$ that originate from a calibration bias. Vectors near the model body additionally are subject to biases from laser glare off the surface, despite the presence of thin mylar strips adhered to the model to reduce light reflection; this is particularly evident in Fig. 7a near the lateral position of the spin-rocket nozzle. One of the most troublesome issues encountered during the experiment was fouling of the windows by oil residue from the smoke. This created light glare in specific locations on the windows and induced notable measurement biases, witnessed in Fig. 7 principally in the lower right region of each vector field (near $y/d_j \approx 6$ and $z/d_j \approx 6$). As the test progressed, the oil film accumulated and the biases became more pronounced. Figure 7b was acquired early in a series of runs and does not display a meaningful oil-induced bias. Figure 7c was acquired next and shows a slight perturbation in this region, followed in time by Fig. 7d, which shows a greater velocity bias in the $+y$ and $-z$ direction. Figures 7a and 7e were acquired subsequently and possess a clear bias in the streamwise component as well as the in-plane effect. Eventually the test would have to be halted, the tunnel shut down, and windows cleaned. If such an event could not coincide with a planned model change, this presented a significant time and financial expense and thus was postponed to the greatest extent possible. Subsequent data analysis revealed more subtle velocity biases as well, attributable to optical interference from the oil accumulation; this is included in the discussion concerning measurement uncertainty below.

Data also were acquired at $M_\infty = 0.95$ and $M_\infty = 1.1$. Because of space limitations, data for $M_\infty = 0.95$ are excluded and only a portion of the $M_\infty = 1.1$ data are shown. Figure 8 displays vector fields for $J = 16$ and Fig. 9 for $J = 36$, each for the three cases of $\alpha = 0$ deg and $\alpha = \pm 4$ deg. In comparison with the $M_\infty = 0.8$ data in Fig. 7, the vortices in Fig. 8 are smaller but stronger and the streamwise velocity deficits are greater (note that the vector and contour scales are different from Fig. 7 to Fig. 8). It also is apparent that the lower vortex in the CVP possesses a stronger streamwise velocity deficit than the upper vortex, whereas at $M_\infty = 0.8$ the opposite was true. Figure 8 shows that the behavior of the vortices as a function of the angle of attack is more complex than that seen at $M_\infty = 0.8$ in Fig. 7. In Fig. 8b at $\alpha = 4$ deg, the CVP retains much the same appearance as the CVP at $\alpha = 0$ deg in Fig. 8a; however the $\alpha = -4$ deg data in Fig. 8c show that the lower vortex in the CVP has moved closer to the vehicle surface with respect to $\alpha = 0$ deg and has relocated laterally toward the vehicle centerline, such that the two vortices comprising the CVP nearly are stacked vertically. This behavior was not evident in Fig. 7d for $M_\infty = 0.8$. It also is noteworthy in Fig. 8c that the HSV no longer is obviously discernible.

Similar behavior is evident at $J = 36$ in Fig. 9. Again the vortices for $M_\infty = 1.1$ are smaller and stronger than the comparable $M_\infty = 0.8$ data in Fig. 7e, although the streamwise velocity deficit has

approximately the same magnitude. Figure 9b shows that at $\alpha = 4$ deg, the lower vortex in the CVP has moved closer to the upper vortex compared with Fig. 9a. The $\alpha = -4$ deg data in Fig. 9c mimic the behavior seen for the matching $J = 16$ case in Fig. 8c, wherein the CVP vortices become nearly vertical with the lower vortex having shifted laterally compared with its typical position at $\alpha = 0$ deg. Again the HSV is not apparent in Fig. 9c, possibly suggesting that an interaction between the HSV and the lower CVP

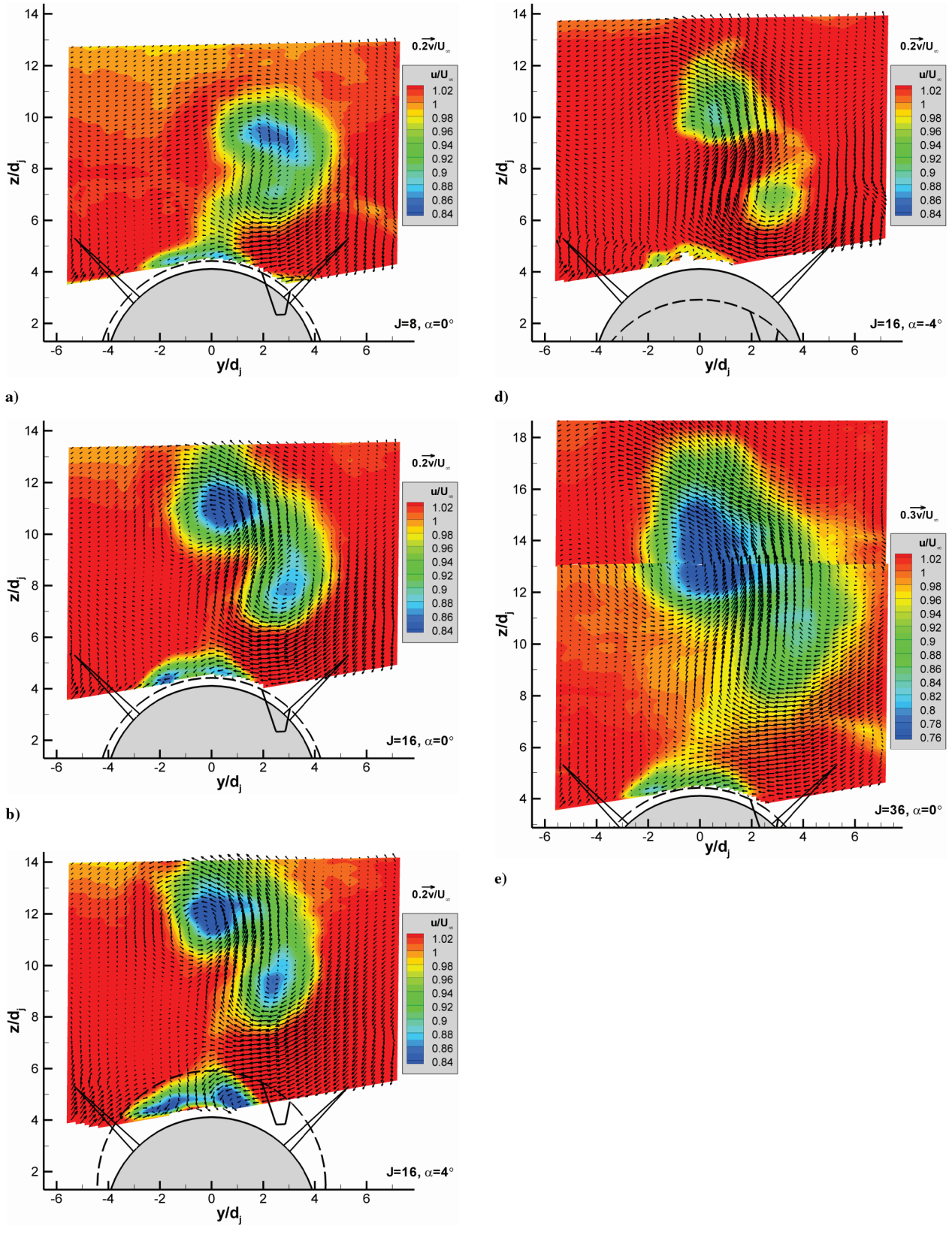

Fig. 7 Mean velocity data at the downstream sheet location for $M_\infty = 0.8$. Vectors represent in-plane velocities and contours the out-of-plane component.

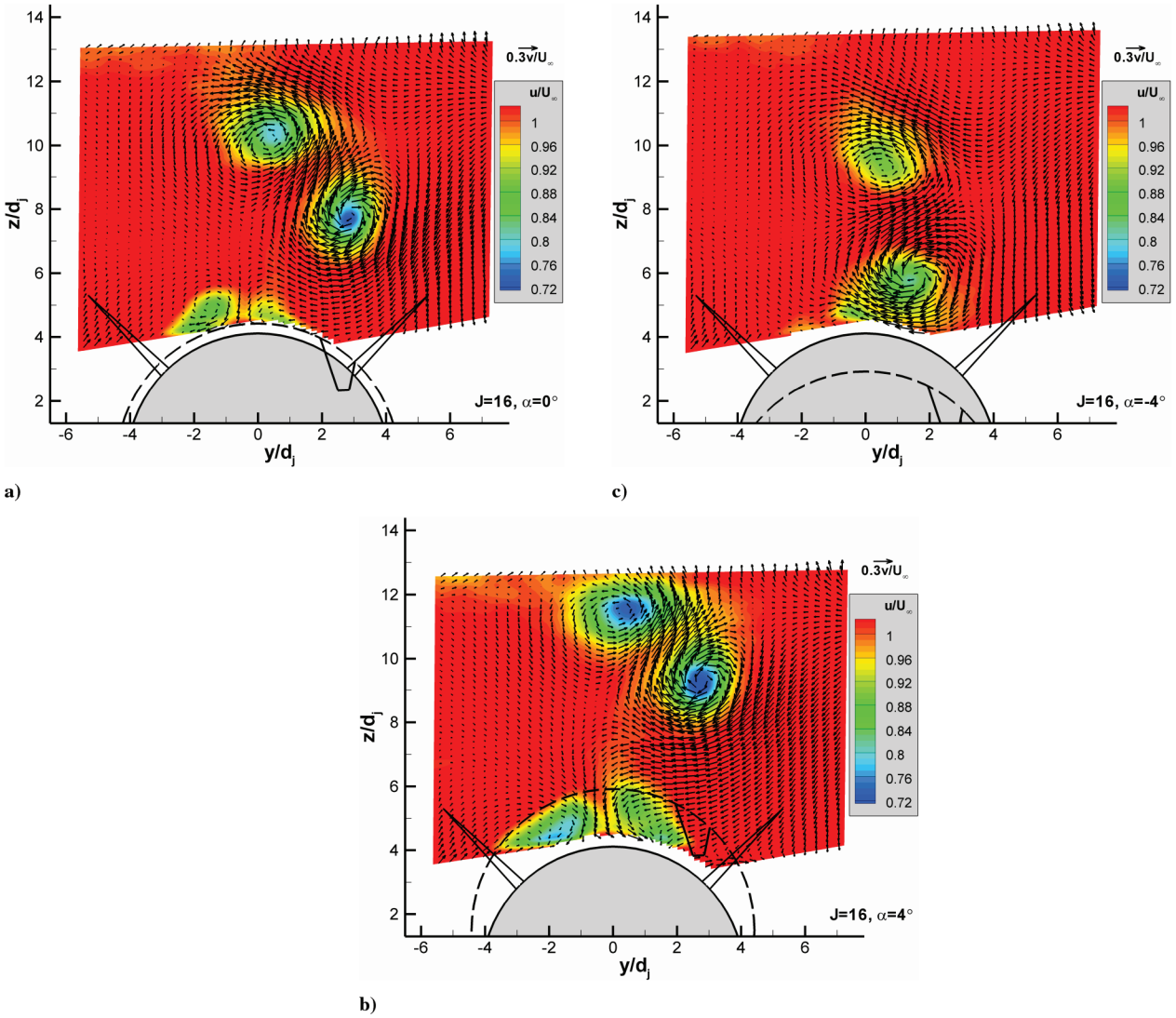

Fig. 8 Mean velocity data at the downstream sheet location for $M_\infty = 1.1$ and $J = 16$.

vortex has occurred to explain the differing vortical structure for the windward cases. Behavior similar to that of Figs. 8c and 9c was observed in the $M_\infty = 0.95$ data, demonstrating a clear trend of the lower vortex in the CVP on the windward side moving closer to the vehicle surface while the HSV becomes undetectable.

Upstream Velocity Fields

Although the large majority of data were collected just upstream of the fins, a small set of data solely at $M_\infty = 0.8$ was acquired at a measurement station 406 mm (16.0 in.) farther upstream, which is still 414 mm (16.3 in.) downstream of the jet nozzle centerline. A separate calibration of the PIV system was conducted at this location.

Data are shown in Fig. 10 at $\alpha = 0$ deg. At this location, the body diameter is closer to the maximum vehicle diameter than at the downstream station. In all three cases, the CVP and HSV have the same essential structure as that observed in Fig. 7, but their size is smaller, sufficiently that the $J = 36$ case can be captured by a single PIV field. The strength of the vortices is substantially greater at the upstream location, seen both in the in-plane velocity magnitudes and the streamwise velocity deficit. The apparent lifting of the HSV off the model surface is likely a result of measurement error due to laser flare from the surface. Unfortunately this measurement station is not sufficiently far upstream to provide data on how the asymmetric CVP orientation with respect to the surface is established following exit from the jet nozzle. The upstream position was limited by the traverse distance of the translation stages, and time and funding limitations did not allow manual relocation of the laser and cameras.

Volume Scan

A data set was gathered at positions 25 mm (1.0 in.) apart spanning the distance from the upstream to the downstream measurement stations for the case in which $M_\infty = 0.8$, $J = 16$, and $\alpha = 0$ deg, thus sweeping out a volume of the interaction to track the downstream evolution of the vortices. The laser sheet and cameras were translated in tandem and the calibration was assumed to move with them; a comparison between data processed using the calibration conducted at the upstream station versus the downstream revealed velocity differences well within the experimental uncertainties (see below). Figure 11 shows the resulting 17 planes of data stacked on a three-dimensional contour of the vehicle surface. Only the streamwise velocities are shown. The lower portion of the figure elongates the body axis by a factor of 10 to disperse the measurement planes for clarity.

Examining the data planes from the upstream end to the downstream, the CVP can be seen to grow spatially while the magnitude of the streamwise velocity deficit diminishes. No rotation of the CVP over this range is visually obvious. Quantitative confirmation of this behavior was found by tracking the vortex positions (see below) from one plane to the next, which reveals no discernible lateral motion of either vortex with downstream distance, but both do move farther away from the surface with approximately

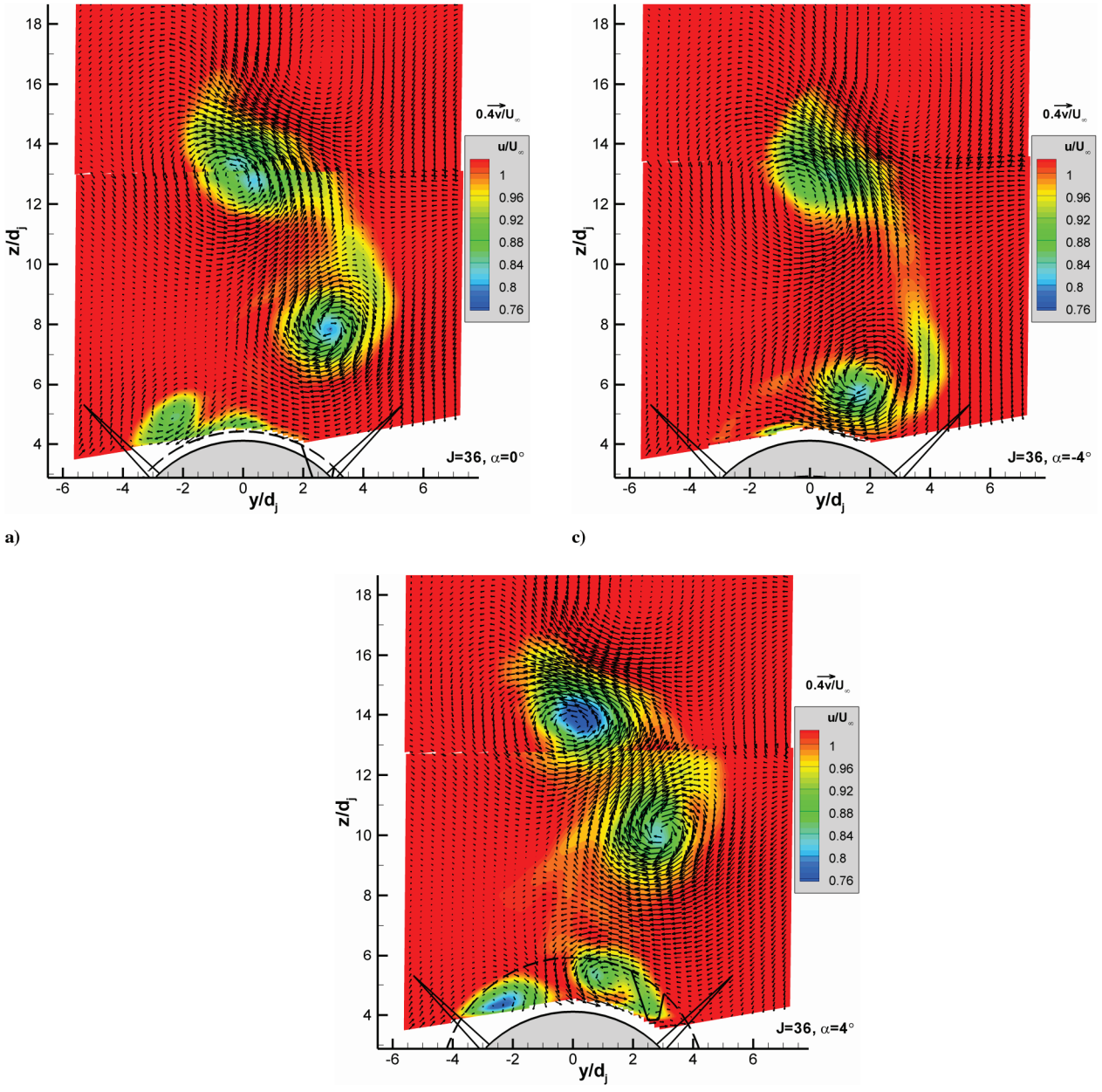

Fig. 9 Mean velocity data at the downstream sheet location for $M_\infty = 1.1$ and $J = 36$.

identical trajectory slopes. This suggests that no rotation of the CVP occurs in this range of downstream planes and that the orientation of the asymmetric CVP must be established near the jet nozzle. No further analysis of the volume scan is addressed within the scope of the present document.

Measurement Uncertainty

Experimental uncertainties were estimated by examining the velocities from six different data runs acquired for the case where $M_\infty = 0.8$, $J = 16$, and $\alpha = 0$ deg. Excepting those $J = 36$ cases where two runs were necessary to cover the spatial extent of the interaction, these are the only repeat runs for the PIV experiment. Mean velocity data were extracted over fields of view common to all six runs, then the uncertainty was found as the 95% confidence interval of the deviations between them. This yields an estimated uncertainty in the mean velocity of ± 11 m/s each in v and w and ± 13 m/s in u. The mismatch between the two PIV vector fields for the $J = 36$ cases lies within these uncertainty estimates. These uncertainties are precision errors and do not include potential biases common to all runs, but an estimate of the in-plane bias error can be derived from a measurement made of the freestream velocities with the model translated well out of the field of view and the jets off. Such freestream data show values of v and w typically reaching about 12 m/s but occasionally as high as 20 m/s. Given that these in-plane velocities are not consistently in one direction, and furthermore that the wind tunnel's flow angularity has been shown to be less than 0.25 deg [19], it can be assumed that this apparent lateral motion in the freestream is not physically real and instead originates from measurement bias. As these values are somewhat in excess of the computed run-to-run precision error, they therefore suggest an additional bias error in some regions of the measurement plane.

A related experiment in a small-scale blowdown wind tunnel similarly detected in-plane PIV bias errors using measurements of the freestream, then used them to correct the bias error in the jet interaction velocity fields [13]. The same approach was determined to be untenable in the present work, however, because the bias errors were not constant throughout the test. Rather as oil accumulated on the windows, in addition to the effects of the light glare described earlier, a small degree of optical interference with the scattered light

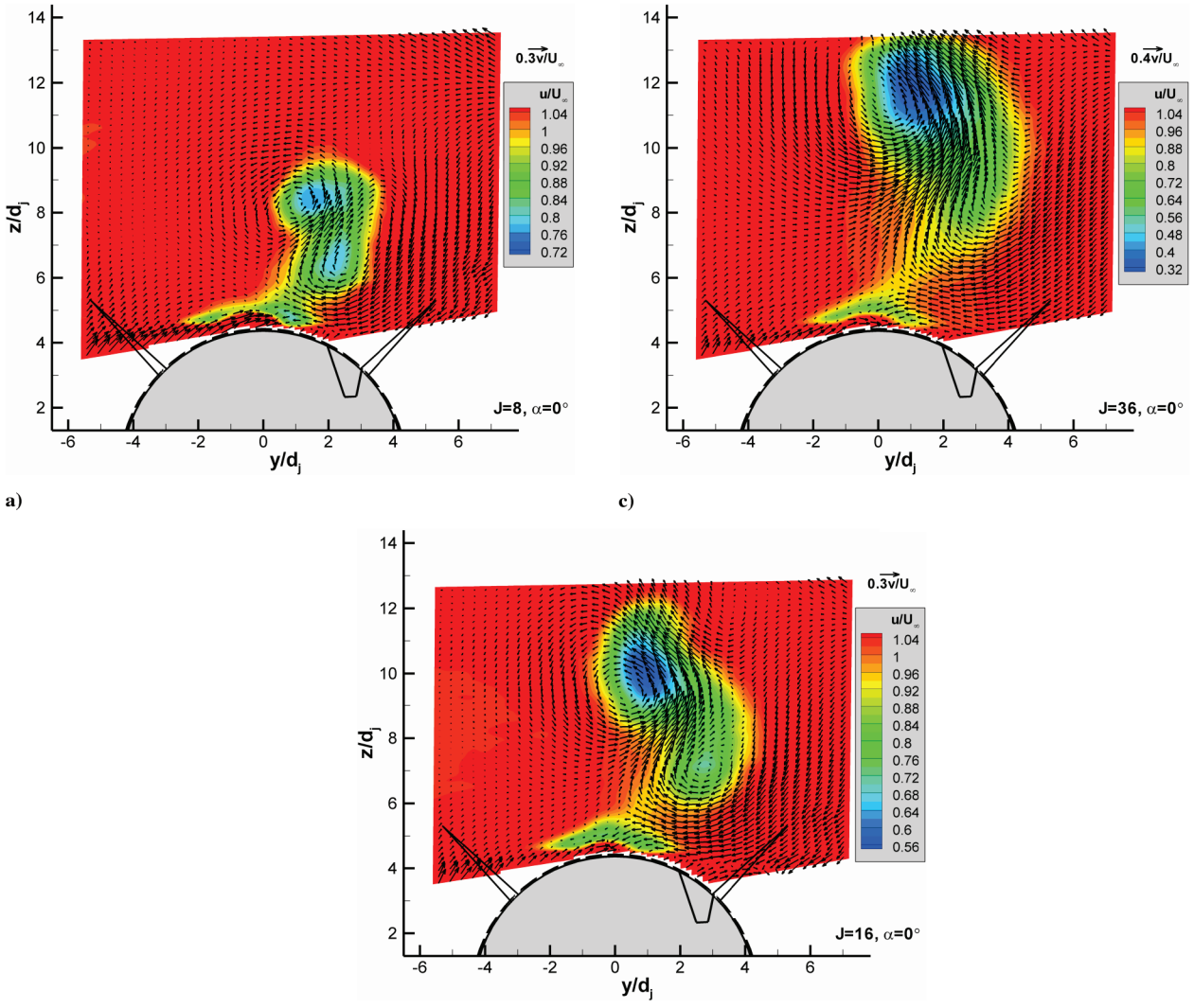

Fig. 10 Mean velocity data at the upstream sheet location for $M_\infty = 0.8$.

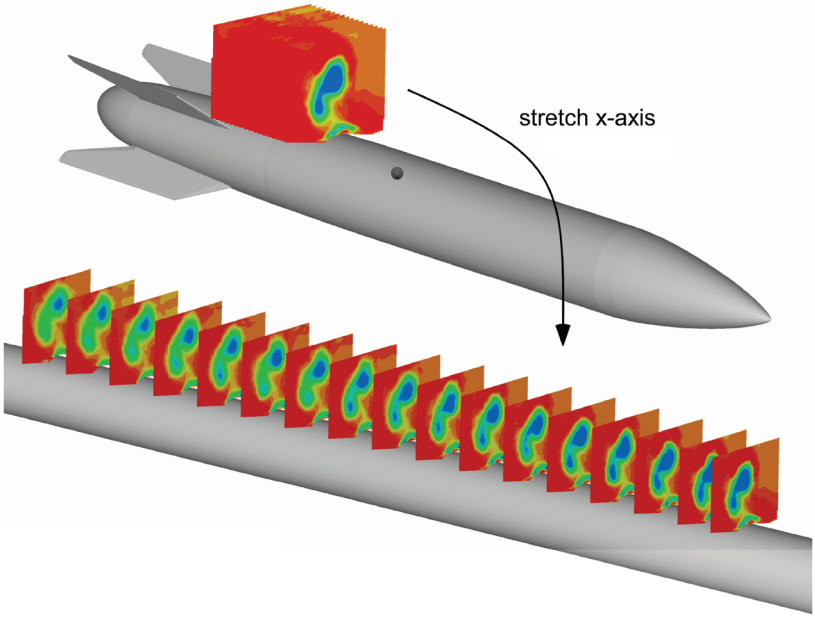

Fig. 11 Mean streamwise velocity data at multiple downstream measurement planes for $M_\infty = 0.8, J = 16$, and $\alpha = 0$ deg. The lower plot elongates the body axis by a factor of 10 for visual clarity.

occurred. This created a subtle and gradual shift from the recorded camera calibration and hence changed the bias errors to values for which correction data were not available. As the six data runs repeating the $M_\infty = 0.8, J = 16, \alpha = 0$ deg case were dispersed in time, these velocity biases due to oil accumulation shifted as well and their impact is included in the uncertainty estimates quoted above.

Data Analysis

Vorticity fields of the crossplane motion are easily calculated from the in-plane velocities using a finite-difference scheme. However because vorticity is a derived quantity, the precision error from the velocity vectors becomes magnified; this difficulty is particularly acute in the present data given the relatively small quantity of instantaneous realizations used in the averages. The most successful means of reducing the noise in the vorticity fields has been found to be increasing the size of the PIV interrogation windows from 32×32 pixels to 64×64 pixels, which essentially trades spatial resolution for velocity precision. Figure 12 shows the mean vorticity field for the $M_\infty = 0.8, J = 16, \alpha = 0$ deg case whose velocity field was shown in Fig. 7b, and it demonstrates that even this effort in noise reduction is limited in its success. Nevertheless each vortex in the CVP is clearly identified but the HSV is virtually undetectable due to the weak in-plane motion associated with it and the difficulty of acquiring measurements near the model surface. Other vorticity fields are anticipated by their velocity fields and are not provided in the interest of brevity.

Despite the noise inherent in the derived vorticity fields, they are useful for determining key characteristics of the CVP. The strength, size, and position of each of the two vortices can be found by employing an integration of the vorticity magnitude for each vortex. The integrated vorticity Γ_x (i.e., the circulation) was computed as per

$$\Gamma_x = \int \omega_x \, \mathrm{d}A \tag{2}$$

by numerically integrating the measured vorticity field over an area whose perimeter was defined by first locating the locus of points 37% $(1/e)$ of the maximum vorticity for that particular case, then extending the perimeter until the slope at each point intersected zero vorticity to better capture the entirety of the vortex. This threshold is somewhat arbitrary in that it was selected not for any physical reason, but because it was found to consistently produce a sensible definition of the vortices; lower thresholds tended to incorporate noise from the vorticity field. The same approach was used in [13] and found to produce results comparable to a paraboloid fit to the peak of the vorticity field, lending credence to this perimeter selection. The centroid of the vortex was found over the same perimeter by

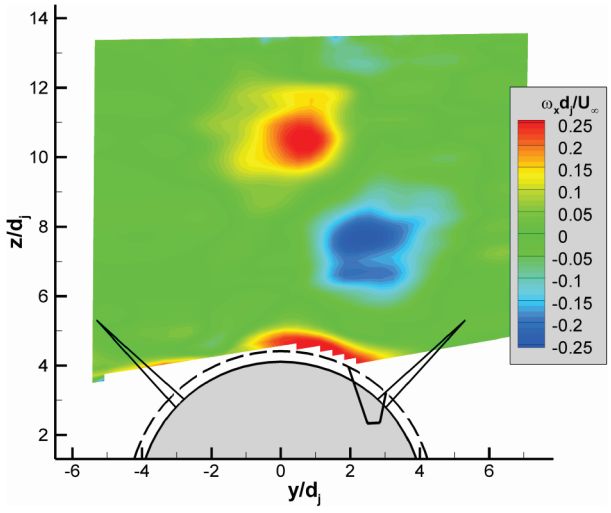

Fig. 12 Mean vorticity field derived from the velocity data of Fig. 7b where $M_\infty = 0.8, J = 16$, and $\alpha = 0$ deg.

$$(\bar{y}, \bar{z}) = \frac{1}{\Gamma_x} \int (y, z) \omega_x \, \mathrm{d}A \tag{3}$$

The vortex diameter was determined by integrating the area over the circulation contour, then computing the diameter as if the vortex were circular.

The resulting vortex centroid positions are shown in Fig. 13, in which the two vortices are discriminated by the sign of their vorticity; the vortex farther from the model surface has positive vorticity (solid data points) and the vortex close to the surface has negative vorticity (empty data points). The data are grouped by J rather than M_∞ because the vortex location was found not to be a strong function of M_∞. When data in Fig. 13 instead are grouped by M_∞, no decipherable pattern emerges. The error in the vortex positions is based upon evaluating the six repeat runs for the case where $M_\infty = 0.8, J = 16$, and $\alpha = 0$ deg. Figure 13 shows that regardless of angle of attack, the positive vortex moves farther from the surface as J is increased, accompanied by a notable lateral movement in the $-y$ direction. Contrarily the negative vortex exhibits significantly less change in position as J is altered.

The circulation for each vortex also may be evaluated for trends versus J and M_∞, the results of which are omitted because they adhere to the anticipated behavior: the magnitude of $\Gamma_x/(d_f/U_\infty)$ rises as J is increased and is larger for greater M_∞. Similarly the vortex diameter is found to increase with J and diminish with M_∞. Neither the circulation magnitude nor the vortex diameter is found to be consistently larger for one of the two vortices in the CVP compared with the other.

The greater proximity of the negative vortex to the vehicle's fins as compared with the positive vortex, coupled with its relatively stable position regardless of M_∞ and α, suggests that the circulation of the negative vortex should have the greatest influence upon the forces seen by the fins. Therefore it is reasonable to posit that a relationship exists between this circulation and the countertorque experienced by the vehicle. This is shown by Fig. 14, which plots the normalized circulation of the negative vortex against the countertorque coefficient C_{CT} measured simultaneously by the balance, without regard for J or M_∞. Data are shown only for $\alpha = 0$ deg because cases at angle of attack are formed by the addition of two interactions, one on the windward side and one on the leeward side, and hence a single value of circulation cannot be determined. A clear correlation is evident, exceeding the uncertainty of the measurement, and indicates that the strength of the negative vortex is a determining factor in the jet/fin interaction. One data point, marked in Fig. 14, can be considered an outlier. Although it is only modestly off the trend of the data, the velocity field data show that for this case the negative vortex appears to interact with the HSV and is pulled into greater proximity with the vehicle surface. This appears to occur regularly on the windward side when the model is pitched to angle of attack, particularly at higher values of J, and can be seen in Figs. 8c and 9c, but this phenomenon does not occur at $\alpha = 0$ deg for any case in the entire data set except the sole data point indicated in Fig. 14. This outlier, and the apparent cause of its occurrence, becomes relevant later in the data analysis.

Because the vortex circulation is a quantity integrated from the velocity field, this suggests that a more fundamental relationship with countertorque can be found in the motion generated by the vortex. It previously has been suggested that the countertorque may be viewed as resulting from an angle of attack on the fins induced by the vorticity of the CVP [7]. This theory was examined by extracting the velocities very near the fin on the $+y$ side of the model (the interaction of the CVP with the fin on the $-y$ side has been shown to be negligible from pressure taps on each fin) and computing the angle of attack with respect to the fin. Figure 15 compares this value, α_{fin}, to C_{CT} and finds no discernible correlation, again examining data only at a vehicle angle of attack of $\alpha = 0$ deg. Adjusting the region in which velocities were extracted did not meaningfully change the results, although the laser sheet position and optical interference from the vehicle surface place limits on the portion of the fin over which valid velocity vectors may be found. Nevertheless computation of the uncertainty in α_{fin} clearly demonstrates that if

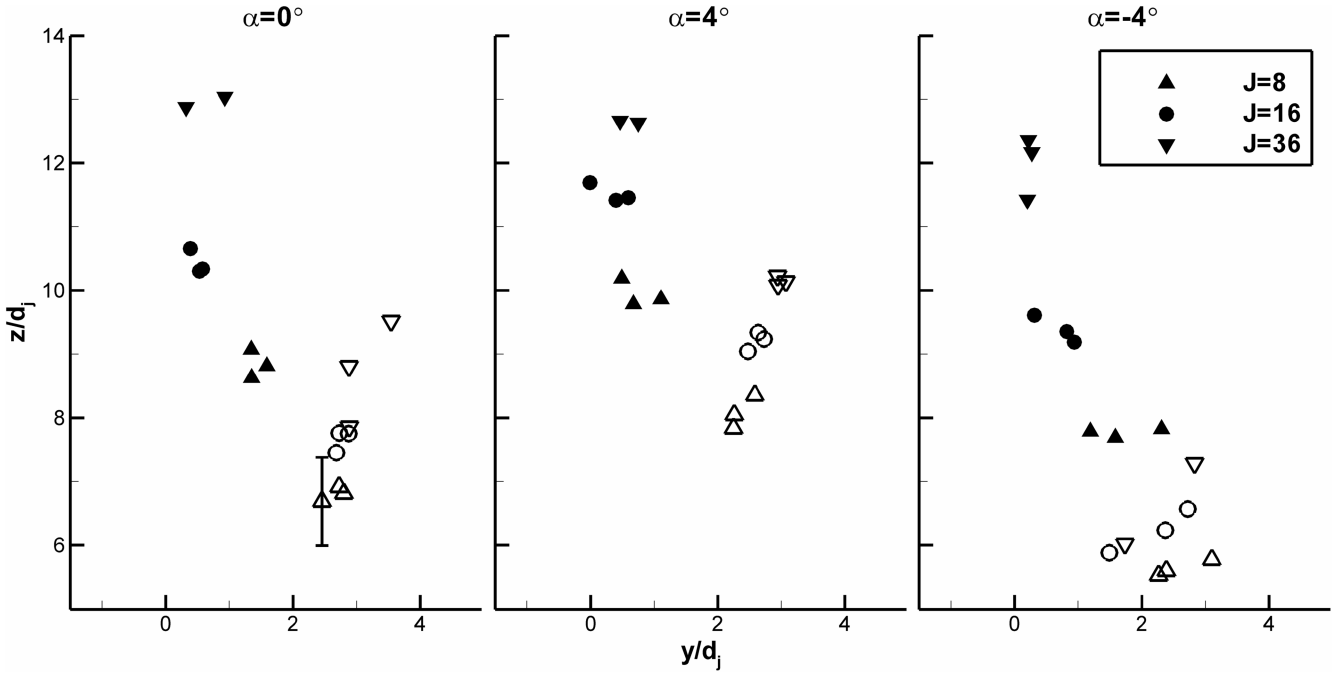

Fig. 13 Positions of the CVP vortices found from the vorticity centroids. The positive vortex (far from surface) is shown by solid data points and the negative vortex (near surface) is shown by empty data points. All Mach numbers are grouped together.

such a correlation does exist, it is too subtle for the accuracy of the present measurements. Highlighting this point are the negative values of α_{fin} commonly found in Fig. 15, which are physically implausible because C_{CT} is never found to be negative. To further emphasize this point, the plot shows several data points that were acquired for cases with the jet off, that is, $J = 0$, in which α_{fin} must be zero because no vortices form to create lateral motion ($\alpha = 0°$ for these cases, precluding the possibility of an effect from body vortices generated near the vehicle nose). The nonzero values found at $J = 0$ emphasize the difficulty of determining α_{fin} with sufficient precision to identify a trend with C_{CT}.

At first encounter, it may appear odd that the PIV measurement biases would mask a correlation between C_{CT} and α_{fin} but not circulation, given that both are quantities derived from the velocity field. However consideration of the error sources provides an explanation. Determination of α_{fin}, as it occurs over a narrow region in proximity to the model surface, is subject to localized errors due to laser flare and oil reflection, whereas circulation is integrated over a large quantity of individual velocity vectors and thus mutes the effect of such errors. Furthermore the gradual alteration of the camera calibration biases by optical interference of the scattered light through the oil film accumulated on the windows leads to a subtle shift in the measured velocities over time, which will not correlate with any physical property. These calibration biases are typically of low spatial frequency, therefore when the vorticity is calculated the biases tend to cancel out through the derivative computation. Although the precision error rises in the vorticity as compared with the velocity, the reduction of the calibration biases is a dominating effect, and hence, the vorticity field is less subject to error than the velocity field from which it is derived.

Vortex Modeling

Given that the vorticity field appears to provide more reliable results than the velocity field for correlation with the countertorque

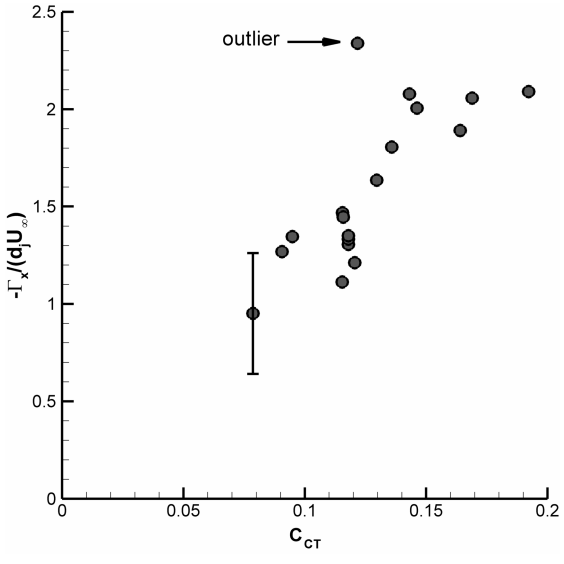

Fig. 14 Circulation of the negative vortex in the CVP plotted against the countertorque coefficient. All data at $\alpha = 0$ deg.

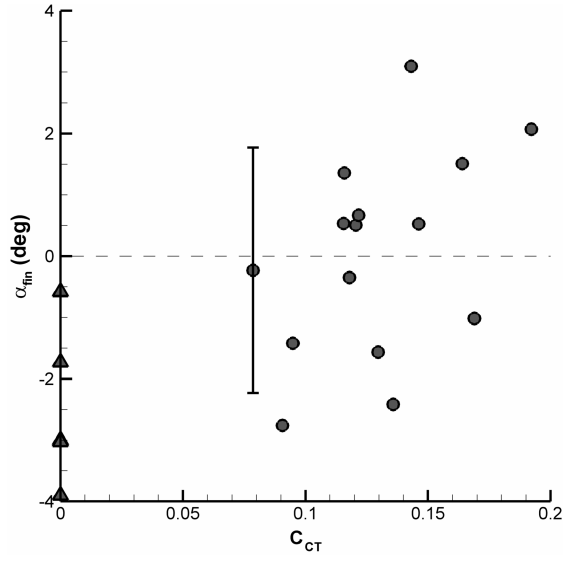

Fig. 15 Angle of attack induced upon a fin by the CVP plotted against the countertorque coefficient. All data at $\alpha = 0$ deg. Triangles represent data for $J = 0$.

data, but that the fundamental source of jet/fin interaction is believed to lie in the velocity data, the question is posed whether the velocities may be reconstructed using the vorticity data to create a new, unbiased field. A possible approach to accomplish this is to take the key attributes for each vortex determined from the vorticity field as described above, then use these values as parameters in a model of the velocity field generated by a jet-in-crossflow. Based upon the approach of Fearn and Weston [20], a diffuse vortex model was constructed wherein each vortex in the CVP is assumed to be symmetric and have a Gaussian distribution; the HSV is not modeled. The superposition of these two vortices determines the velocity field as per

$$\boldsymbol{V} = \frac{1}{2\pi}\left\{\frac{a_1\Gamma_{x1}}{r_1}\left[1-\exp\left(-\frac{b_1^2 r_1^2}{d_{\Gamma 1}^2}\right)\right]\hat{e}_{\theta 1} + \frac{a_2\Gamma_{x2}}{r_2}\left[1-\exp\left(-\frac{b_2^2 r_2^2}{d_{\Gamma 2}^2}\right)\right]\hat{e}_{\theta 2}\right\} \tag{4}$$

where Γ_{x1} and Γ_{x2} are the circulations of the two vortices as found from Eq. (2), $d_{\Gamma 1}$ and $d_{\Gamma 2}$ are their diameters, and a_1, a_2, b_1, and b_2 are constants that are adjusted to fit the model results to the measured vorticity field. As defined in Fig. 16, r_1 and r_2 are the distances from a particular point to each vortex centroid and $\hat{e}_{\theta 1}$ and $\hat{e}_{\theta 2}$ are the unit velocity vector directions. The vortices themselves are located by the measured centroid positions at s_1 and s_2 from the origin of the coordinate axes. Any inclination of the vortices' longitudinal axes with respect to the measurement plane is assumed to be negligible. The constants are chosen for each flowfield case to match the modeled vorticity field to the measured one; these constants help account for the fact that the vortices are not actually circular and the pragmatic but physically arbitrary choice of the vortex perimeter.

In the course of comparing the vortex model results with the measured velocity fields, it became apparent that using the two-vortex model described above created a nonphysical flow through the vehicle surface when the negative vortex was located near it. As a correction, an image vortex was added inside the model body for each of the two CVP vortices, using circulations of identical magnitude but inverse sign to the original vortex and positions as described by Nielsen [21]

$$s_3 = \frac{d_x^2}{4s_1} \quad \text{and} \quad s_4 = \frac{d_x^2}{4s_2} \tag{5}$$

where d_x is the diameter of the vehicle body at the location of the PIV measurement plane. The image vortex diameters are found from

$$d_{\Gamma 3} = \frac{d_x^2 d_{\Gamma 1}}{(2s_1 - d_{\Gamma 1})(2s_1 + d_{\Gamma 1})} \quad \text{and} \quad d_{\Gamma 4} = \frac{d_x^2 d_{\Gamma 2}}{(2s_2 - d_{\Gamma 2})(2s_2 + d_{\Gamma 2})} \tag{6}$$

which may be derived by inserting points along the vortex perimeter into Eq. (5). Unfortunately this four-vortex model, although successful in treating the flow through the vehicle surface, created a strong upwash against the fin on the $-y$ side of the model, which is known not to be correct both from the PIV velocity fields (the upwash seen to varying degrees in vector fields in Figs. 7–10 has been shown to be a calibration bias) and from pressure taps on the fins during the earlier wind-tunnel experiment [7]. As an alternative, a three-vortex model was used in which only the negative vortex was imaged, on the premise that only this vortex is sufficiently close to the surface to require imaging. This approach was found to produce a consistently plausible model of the flowfield.

Figure 17 displays the three-vortex model results for the case where $M_\infty = 0.8$, $J = 16$, and $\alpha = 0$ deg, corresponding to the PIV measurement shown in Fig. 7b and the derived vorticity in Fig. 12. The modeled and the measured flowfields can be seen to be qualitatively alike, but a more direct comparison is appropriate. The line drawn in Fig. 17 passes through the centroid of each vortex, from which a vorticity profile was extracted and is shown in Fig. 18 alongside a comparable profile from the measurement of Fig. 12. As can be seen, the vorticity profile from the vortex model well represents that of the data, but provides a smoother, more idealized profile. This may be regarded as either a simplification of complexities found in the actual flowfield or a removal of measurement errors, or some combination thereof. A comparison of the velocities near the affected fin in the model of Fig. 17 with the data of Fig. 7b reveals that they are in fact substantially different, demonstrating that the model does yield new information, which is expected to be free of PIV bias errors. It must be emphasized that the vortex model is not intended to necessarily provide a complete representation of the vortex structure of the interaction; rather, it has the narrower goal of providing more accurate velocities near the fin.

Using the velocities generated by the three-vortex model as applied to all cases examined by PIV, it is now possible to seek a correlation with the countertorque free of the velocity bias errors that plagued the earlier attempt of Fig. 15. Velocity vectors were extracted from the model velocity field at the midpoint of the fin most affected by the interaction and α_{fin} was calculated from it; the results presented below were substantially the same when α_{fin} was instead determined from the average of velocity vectors across the span of the fin. As before, only cases where $\alpha = 0$ deg were examined so that symmetry could be assumed between the two jet nozzles, and the

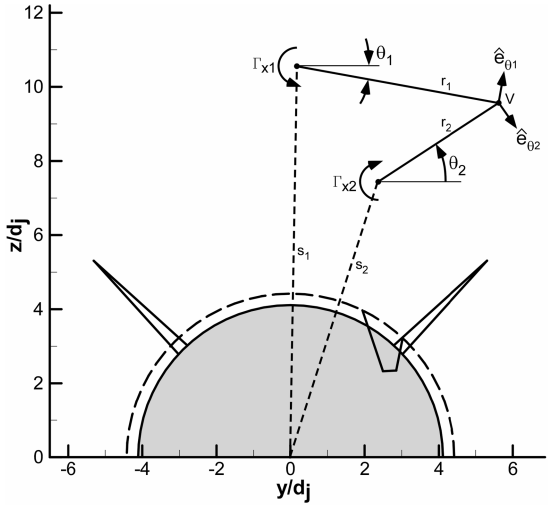

Fig. 16 Definition of geometry for the vortex model.

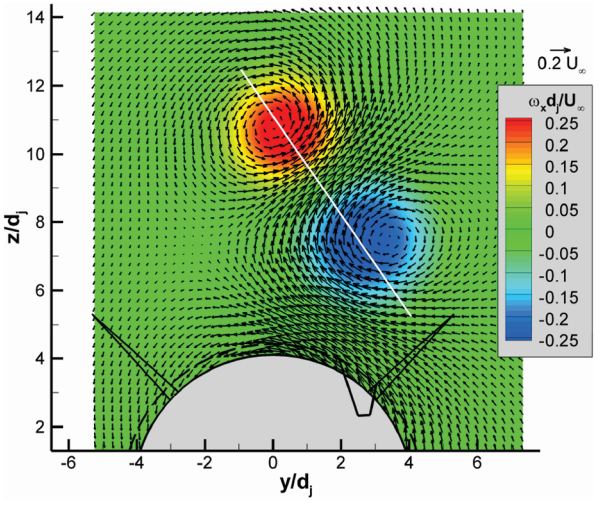

Fig. 17 Results from the three-vortex model for $M_\infty = 0.8, J = 16$, and $\alpha = 0$ deg based on the data of Figs. 7b and 12. The line drawn passes through both vortex centers.

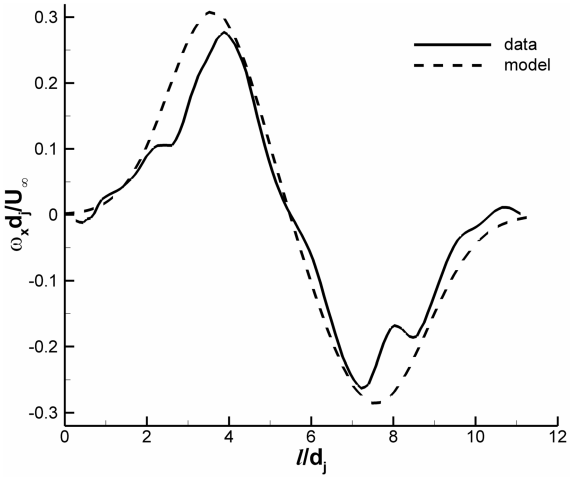

Fig. 18 Vorticity profiles extracted along the line shown in Fig. 17 of both the PIV data and the three-vortex model for $M_\infty = 0.8, J = 16$, and $\alpha = 0$ deg. The distance l is measured from an arbitrary origin.

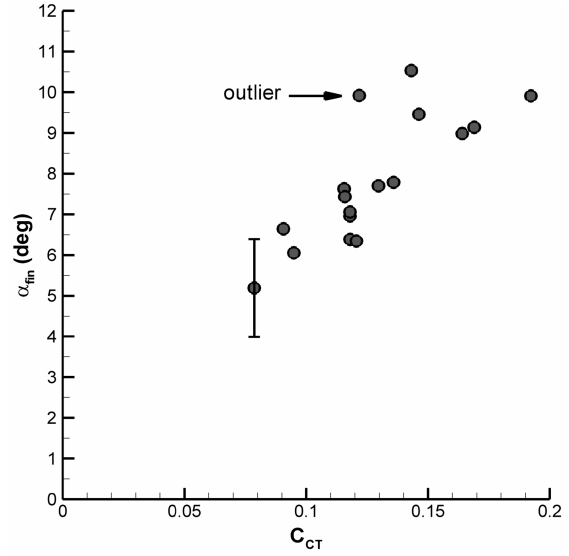

Fig. 19 Angle of attack induced upon a fin by the CVP as found from the three-vortex model plotted against the countertorque coefficient. All data at $\alpha = 0$ deg.

resulting relationship between α_{fin} and C_{CT} is given in Fig. 19. Now a distinct correlation is found, indicating that the jet/fin interaction can be perceived as arising from an induced angle of attack on the fins due to the presence of the CVP. The estimated uncertainty was found by examining the repeatability of the vortex model applied to the six duplicated measurements for the $M_\infty = 0.8, J = 16, \alpha = 0$ deg case and hence does not include questions regarding the model's ability to replicate the actual flowfield. The outlying data point identified in Fig. 14 is still present in Fig. 19, suggesting that the physical effect influencing this point that was not captured in the correlation with circulation is not present in the vortex model either.

A particular angle of attack induced upon a fin cannot be expected to produce identical countertorques regardless of M_∞ or q_∞ because the roll torque of the flight vehicle is not constant across such conditions even when the jets are not operating. A more appropriate connection with C_{CT} instead may be found if α_{fin} can be converted to a roll torque, which would require the creation of a response curve of roll moment as a function of α_{fin} for all flowfield conditions. Fortunately such information may be found from the aerodynamic test of the flight vehicle if additional assumptions are made. The PIV measurements were acquired with a fin cant of 0 deg, at which the expected zero roll moment was measured by the balance when the jets were off, but the aerodynamic tests also included balance measurements at identical flow conditions except with a fin cant of

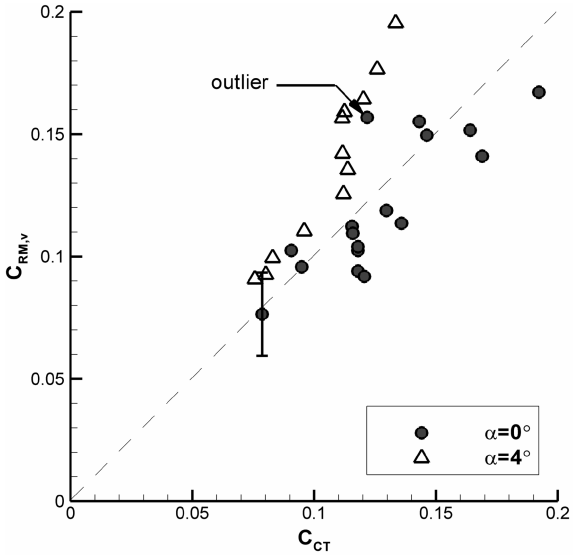

Fig. 20 Rolling moment due to jet/fin interaction based upon the vortex model of the PIV data, $C_{RM,v}$, compared with the countertorque measured by the balance, C_{CT}.

2 deg. Assuming a linear response between these two points, a relationship between the roll moment and α_{fin} can be generated, regardless of whether α_{fin} results from fin cant or vortical motion. Although linearity may be a flawed assumption, in the face of the simplifications already made in the use of the vortex model, it may be sufficiently accurate to provide useful results. Now values of α_{fin} found from the vortex model velocity fields may be converted to the roll torque due to jet/fin interaction based upon the PIV data, $C_{RM,v}$, which is distinct from C_{CT}, the roll torque due to the interaction as measured by the balance. These results are shown in Fig. 20 by the solid circles and yield a correlation much like that found with α_{fin} in Fig. 19; the similarity occurs because the response of the roll moment with α_{fin} changes only by about 10–15% as M_∞ and q_∞ are varied. It is particularly noteworthy that the correlation is close to the ideal one-to-one correspondence marked by the dashed line in Fig. 20, given the numerous assumptions inherent in the use of the vortex model, and this tends to validate the three-vortex model used for the analysis.

Calculation of the effects of the interaction for cases where the vehicle is at angle of attack is now possible using the conversion from α_{fin} to $C_{RM,v}$, as the roll moment may be found independently for the windward and leeward sides of the vehicle and then added together. This assumes symmetry when the model is pitched to either $\alpha = 4$ or $\alpha = -4$ deg, which is known not to be correct when $M_\infty = 0.95$ or 1.1, but this is yet one more assumption among many required to bring the present data analysis to this point. The resulting values of $C_{RM,v}$ for cases where the vehicle is at $\alpha = 4$ deg are shown by the hollow triangles in Fig. 20. Again a strong correlation between $C_{RM,v}$ and C_{CT} is found but at less than the one-to-one correspondence seen for the $\alpha = 0$ deg cases, which suggests that at $\alpha = 0$ deg the CVP is the dominant influence upon the fins but at $\alpha = 4$ deg an additional effect is present in the interaction but not captured by the vortex model. It is instructive that the outlying data point identified earlier for the $\alpha = 0$ deg cases now is found to fit closely with the $\alpha = 4$ deg cases. The connective trait is that most measurements at $\alpha = 4$ deg show that, on the windward side, the negative vortex is pulled close to the vehicle surface by an interaction with the HSV, which also is observed for the outlying case at $\alpha = 0$ deg but no other. This suggests that the role of the HSV is relevant to the prediction of the countertorque in these cases, in which case such effects are explicitly neglected by the vortex model.

Conclusions

A stereoscopic particle image velocimeter has been implemented in the NASA Ames transonic 11-Foot Unitary Plan Wind Tunnel for

studying jet/fin interaction on a full-scale wind-tunnel model of a finned body of revolution. The interaction occurs when the exhaust plumes from spin rockets near the model midbody, simulated in the experiment using high-pressure air, encounter the crossflowing freestream and are redirected downstream where they can alter the forces generated by the vehicle's fins. Data were acquired principally at a measurement plane just upstream of the leading edge of the fin root. The resulting velocity fields clearly display the counter-rotating vortex pair that dominates the far field as well as the remnant of the horseshoe vortex near the vehicle surface. The counter-rotating vortex pair is distinctly asymmetric as a result of having been produced by a jet exiting from a scarfed nozzle and displays some rotation with respect to the model surface. The horseshoe vortex is displaced laterally from the nozzle position.

Data were acquired over a range of flowfield conditions and model orientations, from which key characteristics of the counter-rotating vortex pair were determined by examining the derived vorticity fields. The size and position of each vortex in the pair were found to be chiefly a function of the jet-to-freestream dynamic pressure ratio and that the vortex strength is additionally a function of the freestream Mach number. The vortex of negative sign is always located closer to the fins than its positive counterpart and does not greatly change location as flowfield parameters are altered, which leads to a discovery of a correlation between the circulation of the negative vortex and a reduction in the vehicle roll torque measured simultaneously by an aerodynamic balance. Although this observation coupled with prior studies suggests that the jet/fin interaction arises from an angle of attack induced upon the fins by the vortical motion, further correlations are hindered by untreatable bias errors in the velocimetry.

To circumvent this difficulty, a model of the vortex structure was created to produce new velocity fields free of bias errors based upon key attributes determined from the more reliable vorticity fields. Each vortex in the counter-rotating vortex pair was modeled as a diffuse symmetric vortex possessing a Gaussian distribution and strength, size, and position based upon the vorticity data; the presence of the horseshoe vortex was neglected. The results show a strong correlation between the angle of attack induced upon the fins and the roll torque loss. Further analysis suggests that in level flight the counter-rotating vortex pair provides the dominant effect, but at angle of attack the horseshoe vortex on the windward side has an additional influence.

Overall this study provides an approach to effectively predict the roll torque reduction due to the jet/fin interaction if the properties of the vortex field induced by the jet-in-crossflow interaction are known. It is reasonable to suppose that the same would hold for interactions between upstream and downstream sets of control surfaces found on maneuvering vehicles if the wake of the upstream geometry were adequately understood. However the present work also demonstrates the difficulty of predicting the nature of these vortices, particularly in the transonic regime. Although the fundamental structure expected of a jet-in-crossflow was detected, numerous asymmetries and divergence from the ideal flowfield were found to result from the use of realistic flight hardware, and additional complexities were discovered near sonic flight conditions. Hence this investigation provides significant insight into the mechanism of jet/fin interaction and offers some limited predictive capability, but simultaneously emphasizes the increased understanding of the vortical structure of the flowfield that must be acquired to fully address this problem.

Acknowledgments

This work was supported by Sandia National Laboratories and the U.S. Department of Energy. Sandia is a multiprogram laboratory operated by Sandia Corporation, a Lockheed Martin Company, for the U.S. Department of Energy's National Nuclear Security Administration under Contract No. DE-AC04-94AL85000. The authors would like to thank John Henfling, Carl Peterson, and Walt Wolfe of Sandia National Laboratories for their assistance with experimental planning and data analysis; Rocky Erven, Doug Hodge, and Paul Hooper of Sandia for their wind-tunnel model design and test support; T. Y. Chu, Wahid Hermina, Justine Johannes, Jaime Moya, and Mike Prairie of Sandia for programmatic support; Jennifer Bradley Everett and her wind-tunnel test team at NASA Ames for their extensive efforts; and John Hopf at Arnold Engineering and Development Center for his assistance with the aerodynamic balance.

References

[1] Cassel, L. A., Durando, N. A., Bullard, C. W., and Kelso, J. M., "Jet Interaction Control Effectiveness for Subsonic and Supersonic Flight," U.S. Army Missile Command, Rept. RD-TR-69-21, Redstone Arsenal, Huntsville, AL, Sept. 1969.

[2] Dormieux, M., and Marsaa-Poey, R., "Numerical Assessment of Aerodynamic Interactions on Missiles with Transverse Jets Control," *Computational and Experimental Assessment of Jets in Cross Flow*, CP 534, AGARD, 1993, pp. 30.1–30.11.

[3] Cassel, L. A., "Applying Jet Interaction Technology," *Journal of Spacecraft and Rockets*, Vol. 40, No. 4, 2003, pp. 523–537.

[4] Srivastava, B., "Aerodynamic Performance of Supersonic Missile Body- and Wing Tip-Mounted Lateral Jets," *Journal of Spacecraft and Rockets*, Vol. 35, No. 3, 1998, pp. 278–286.

[5] Brandeis, J., and Gill, J., "Experimental Investigation of Super- and Hypersonic Jet Interaction on Missile Configurations," *Journal of Spacecraft and Rockets*, Vol. 35, No. 3, 1998, pp. 296–302.

[6] Graham, M. J., Weinacht, P., and Brandeis, J., "Numerical Investigation of Supersonic Jet Interaction for Finned Bodies," *Journal of Spacecraft and Rockets*, Vol. 39, No. 3, 2002, pp. 376–383.

[7] Peterson, C. W., Wolfe, W. P., and Payne, J. L., "Experiments and Computations of Roll Torque Induced by Vortex-Fin Interaction," AIAA Paper 2004-1069, Jan. 2004.

[8] Margason, R. J., "Fifty Years of Jet in Cross Flow Research," *Computational and Experimental Assessment of Jets in Cross Flow*, CP 534, AGARD, 1993, pp. 1.1–1.41.

[9] Fric, T. F., and Roshko, A., "Vortical Structure in the Wake of a Transverse Jet," *Journal of Fluid Mechanics*, Vol. 279, 1994, pp. 1–47.

[10] Kelso, R. M., Lim, T. T., and Perry, A. E., "Experimental Study of Round Jets in Crossflow," *Journal of Fluid Mechanics*, Vol. 306, 1996, pp. 111–144.

[11] McCann, G. J., and Bowersox, R. D. W., "Experimental Investigation of Supersonic Gaseous Injection into a Supersonic Freestream," *AIAA Journal*, Vol. 34, No. 2, 1996, pp. 317–323.

[12] Santiago, J. G., and Dutton, J. C., "Velocity Measurements of a Jet Injected into a Supersonic Crossflow," *Journal of Propulsion and Power*, Vol. 13, No. 2, 1997, pp. 264–273.

[13] Beresh, S. J., Henfling, J. F., Erven, R. J., and Spillers, R. W., "Crossplane Velocimetry of a Transverse Supersonic Jet in a Transonic Crossflow," *AIAA Journal*, Vol. 44, No. 12, 2006, pp. 3051–3061.

[14] Beresh, S. J., Henfling, J. F., Erven, R. J., and Spillers, R. W., "Penetration of a Transverse Supersonic Jet into a Subsonic Compressible Crossflow," *AIAA Journal*, Vol. 43, No. 2, 2005, pp. 379–389.

[15] Beresh, S. J., Henfling, J. F., Erven, R. J., and Spillers, R. W., "Turbulent Characteristics of a Transverse Supersonic Jet in a Subsonic Compressible Crossflow," *AIAA Journal*, Vol. 43, No. 11, 2005, pp. 2385–2394.

[16] Samimy, M., and Lele, S. K., "Motion of Particles with Inertia in a Compressible Free Shear Layer," *Physics of Fluids A*, Vol. 3, No. 8, 1991, pp. 1915–1923.

[17] Melling, A., "Tracer Particles and Seeding for Particle Image Velocimetry," *Measurement Science and Technology*, Vol. 8, No. 12, 1997, pp. 1406–1416.

[18] Soloff, S. M., Adrian, R. J., and Liu, Z.-C., "Distortion Compensation for Generalized Stereoscopic Particle Image Velocimetry," *Measurement Science and Technology*, Vol. 8, No. 12, 1997, pp. 1441–1454.

[19] Amaya, M. A., and Murphy, S. V., "Flow Quality Measurements in the NASA Ames Upgraded 11-by-11-ft. Transonic Wind Tunnel," AIAA Paper 2000-2681, June 2000.

[20] Fearn, R., and Weston, R. P., "Vorticity Associated with a Jet in a Cross Flow," *AIAA Journal*, Vol. 12, No. 12, 1974, pp. 1666–1671.

[21] Nielsen, J. N., *Missile Aerodynamics*, McGraw–Hill, New York, 1960, p. 91.

R. Lucht
Associate Editor